

Effect of particle shape on the electrochemical properties of CaSnO_3 as an anode material for lithium-ion batteries

Hyun Sik Kim · Sang-Sun Park · Soon Hyung Kang · Yung-Eun Sung

Received: 6 March 2014 / Accepted: 20 May 2014 / Published online: 6 June 2014
© Springer Science+Business Media Dordrecht 2014

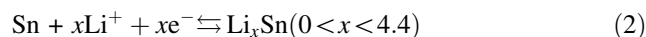
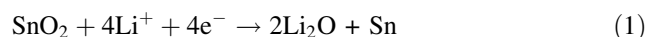
Abstract Cubic and star-shaped CaSnO_3 particles with a perovskite structure were synthesized successfully using a simple hydrothermal method at a low temperature of 140 °C. The structure and morphology of the CaSnO_3 powders were characterized using X-ray diffraction, X-ray photoelectron spectroscopy, and scanning electron microscopy. The electrochemical properties of the CaSnO_3 as anode materials for lithium-ion batteries were tested by constant current discharge/charge and cyclic voltammetry. The large irreversible capacity in the initial cycle was similar to that of tin oxide, due to the decomposition of tin oxide into metallic tin and Li_2O , followed by a reversible Li–Sn formation. The reversible capacity of the cubic CaSnO_3 was 382 mAh g^{-1} in the first cycle and was maintained at 365 mAh g^{-1} in the following cycles. The cubic CaSnO_3 particles had a higher reversible capacity than the star-shaped CaSnO_3 particles and retained a capacity of about 365 mAh g^{-1} after 60 cycles as well as good cycle stability, showing potential as attractive anode materials for lithium-ion batteries. It is found that the

particle shape had a marked effect on electrochemical performance.

Keywords CaSnO_3 nanoparticles · Particle shape effect · Lithium-ion battery · Anode

1 Introduction

Lithium-ion batteries (LIBs) have attracted much attention as suitable power sources for various electronic devices because of their high energy and power densities. In particular, significant interest has been shown in Li-metal alloys (e.g. Si, Sn, Sb, Ge) as anode materials for LIBs due to the higher theoretical capacity and lower operating potential (vs. lithium) than the commercially used carbon anode (370 mAh g^{-1}) [1–4]. As an example, tin oxide (SnO_2) and tin-based composite oxides, having a theoretical capacity of 782 mAh g^{-1} , have received considerable attention as promising anode materials for LIBs, but the volume expansion during the discharging/charging process is still a critical issue to be overcome [5–7]. The following equations show the general mechanism of tin oxides in two steps [8].



Initially, SnO_2 is irreversibly reduced to metallic Sn in the Li_2O matrix and, subsequently, Sn forms an alloy with lithium (Li) during discharging/charging cycling. It has been found that the high cycling stability is maintained because the Li_2O phase acts as a cushion to relieve the volume expansion in the case where the Sn atoms are dispersed [9, 10]. However, substantial capacity fading

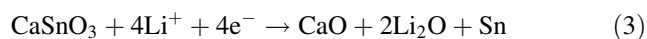
H. S. Kim · S.-S. Park
Energy Material Group, Lotte Chemical, 115, Gajeongbuk-ro,
Yuseong-gu, Daejeon 305-726, South Korea

S. H. Kang (✉)
Department of Chemical Education, Chonnam National
University, Gwangju 500-757, South Korea
e-mail: skang@jnu.ac.kr

Y.-E. Sung (✉)
School of Chemical & Biological Engineering and Research
Center for Energy Conversion & Storage, Seoul National
University, San 56-1, Sillim-dong, Gwanak-gu, Seoul 151-744,
South Korea
e-mail: ysung@snu.ac.kr

during cycling has also been observed, resulting from the aggregation of Sn atoms into clusters. The alloying process induces grains to grow increasingly larger, eventually producing cracking of the electrode and a rapid loss of capacity [11, 12]. Thus, the poor cycling stability and largely irreversible capacity loss, attributed to the large volume expansion during the cycling, have been regarded as major drawbacks [13, 14]. To overcome these limitations, another suitable matrix enabling to buffer to the large volume change during the discharging/charging process would be desirable.

CaSnO_3 has been considered as another possible anode material because a new matrix can be formed by the introduction of Ca ions into SnO_2 , finally improving the cycling performance and preventing the aggregation of Sn particles. That is, the reaction of Li ions with CaSnO_3 induces the formation of Sn, CaO, and Li_2O , followed by the alloying and dealloying process of Sn metal. The related reaction mechanism of CaSnO_3 is as follows [15]:



Further, a reversible Li–Sn alloy is formed following Eq. (2). Here, the CaO and Li_2O phases can act as a physical barrier to suppress the aggregation of Sn particles as well as a cushion to reduce the volume expansion during cycling.

In this work, cubic and star-shaped CaSnO_3 particles were synthesized using a facile hydrothermal method by varying the concentration of polyvinylpyrrolidone (PVP) surfactant. The shape effect of CaSnO_3 anode materials was then analyzed using various electrochemical characterizations.

2 Experimental

All of the reactants and solvents were of analytical grade and were used without further purification. In a typical synthesis, 2.2 mmol of CaCl_2 and 1.6 mmol of $\text{Na}_2\text{SnO}_3 \cdot 3\text{H}_2\text{O}$ were dissolved in 10 mL of distilled (DI) water in a separate beaker. A suitable amount of 0.2 M PVP (MW. 1,300,000) aqueous solution was added to the CaCl_2 solution and two solutions were mixed together under vigorous stirring. The resulting solution was placed into a Teflon-lined stainless steel autoclave with a capacity of 50 mL and was then filled with DI water up to 80 % of the total volume. Subsequently, the autoclave was sealed and maintained at 140 °C for 12 h. After the reaction, a white CaSn(OH)_6 power was collected, washed with DI water several times, and dried in a vacuum at 60 °C for 12 h. Finally, the CaSn(OH)_6 powder was calcined at 800 °C for 5 h under an Ar atmosphere.

The crystal structures of the as-prepared samples were examined by X-ray diffraction (XRD) using a Rigaku diffractometer, operated with a CuK_α radiation source

($\lambda = 1.541 \text{ \AA}$) at an operating voltage and current of 50 kV and 200 mA, respectively. Fourier transform-infrared (FT-IR) spectra, in the range of 900–4,000 cm^{-1} , were obtained on a Nicolet 5700 spectrometer, using the potassium bromide (KBr) pellet technique. The morphology of the resulting products was examined using field emission scanning electron microscopy (FE-SEM, JSM-6330F, JEOL, Japan). X-ray photoelectron spectroscopy (XPS) analyses were performed in a UHV multipurpose surface analysis system (SIGMA PROBE, Thermo, UK), operating at base pressures of $<10^{-9}$ mbar. The photoelectron spectra were excited by an AlK_α (1486.6 eV) anode, operating at a constant power of 100 W (15 kV, 10 mA). The binding energy (BE) scale was calibrated from the hydrocarbon contamination using the C 1s peak at 284.6 eV.

Electrochemical measurements were performed in two electrode cells with lithium foil as both the reference and counter electrodes. The working electrodes were prepared with CaSnO_3 as the active material, Super P as the conducting material, and polyvinylidene fluoride (PVDF) as the binder, mixed at a weight ratio of 75:10:15 and stirred in 1-methyl-2-pyrrolidinone (NMP). The slurry was spread onto Cu foil with a diameter of 10 mm and dried, and then pressed and used as the working electrode. Then, the thickness and coating density of the CaSnO_3 electrode sheet were about 150 μm and 0.7, respectively.

The coin-type half cells were assembled in an Ar-filled glove box using Li foil as the reference and counter electrodes, an organic liquid mixture of ethyl carbonate (EC) and dimethylcarbonate (DMC) at a 1:1 volumetric ratio containing 1 M LiClO_4 as the electrolyte, and polyethylene film (Celgard 2300) as the separator. The cells were charged and discharged at a constant current density of 50 mAh g^{-1} between 0 and 1.0 V versus Li/Li^+ on a Toyosystem TYS-31TU01SCR. Cyclic voltammetry (CV) was carried out in the potential range of 0.0–1.0 versus Li/Li^+ at a scan rate of 0.5 mV s^{-1} on a Solartron Multistat instrument (model 1480).

3 Results and discussion

The synthesis conditions of the CaSnO_3 particles determine the shape and length of the final products and, in particular, the concentration of the PVP surfactant and pH of the synthesis solution were reported based on the hydrothermal method [16–18]. Here, it was found that varying the concentration of the PVP surfactant was the determining factor controlling the shape of the CaSnO_3 particles. Cubic CaSnO_3 particles were prepared using 5 mL PVP surfactant, while the addition of 1 mL PVP surfactant induced star-shaped CaSnO_3 particles. Representative XRD

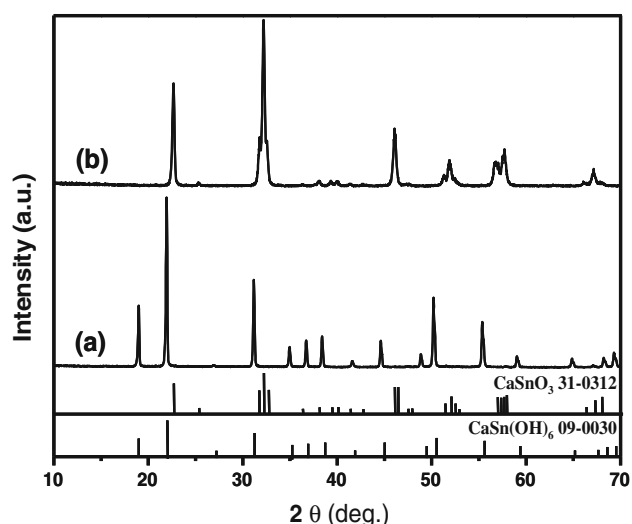


Fig. 1 XRD patterns of **a** the as-synthesized CaSn(OH)_6 particles and **b** CaSnO_3 particles developed after high-temperature thermal treatment at 800 °C for 5 h under Ar

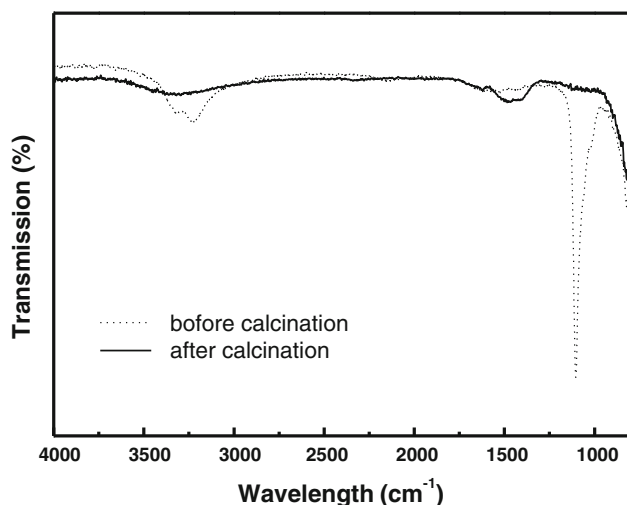


Fig. 2 FT-IR spectra of *cubic* and *star-shaped* CaSnO_3 particles before and after calcination

patterns of the as-synthesized precursor, and the CaSn(OH)_6 and CaSnO_3 particles are shown in Fig. 1. In the case of CaSn(OH)_6 , all peaks in the pattern are clearly indexed to a pure cubic phase of CaSn(OH)_6 . No other impurities were detected in the scanned angle. After the thermal treatment at 800 °C for 5 h, the as-synthesized CaSn(OH)_6 precursor was entirely converted into orthorhombic CaSnO_3 particles (JCPDS 31-0312), as shown in Fig. 1b. No impurities were detected in the patterns and the sharpness and intensity of the XRD peaks indicated that the CaSnO_3 particles exhibited highly crystalline properties. Figure 2 shows the FT-IR spectra of the CaSn(OH)_6 particles before and after heat treatment. Before calcination,

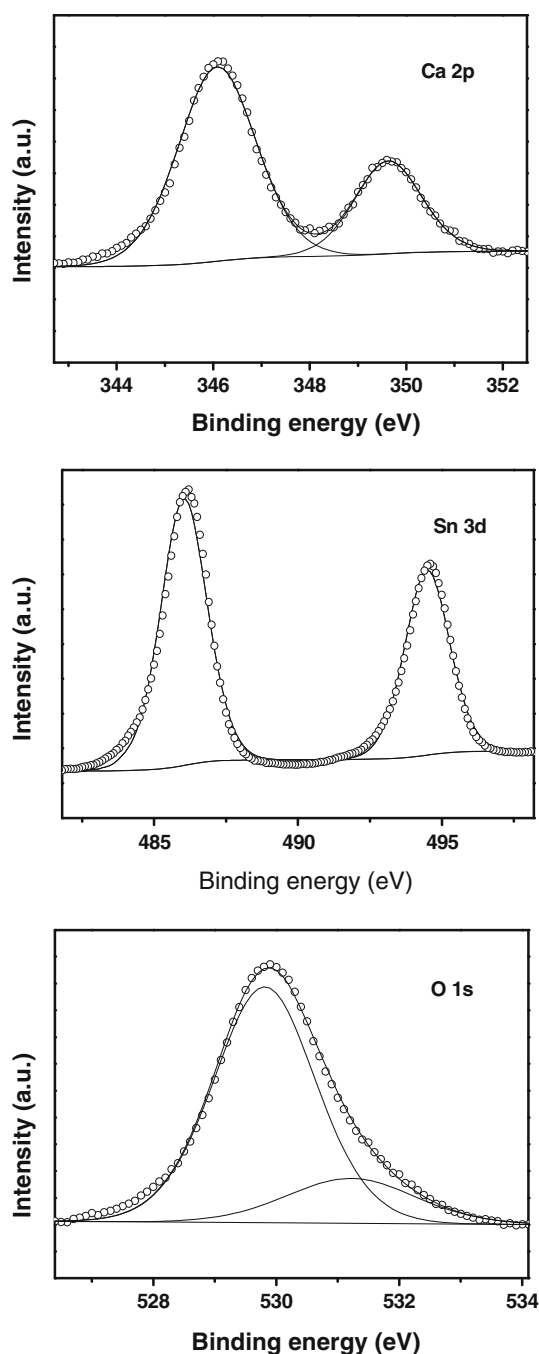


Fig. 3 XPS core-level peaks of Ca 2p, Sn 3d, and O 1s elements in cubic CaSnO_3 particles

IR peaks were observed in two regions. In particular, a broad band at $\sim 3,300 \text{ cm}^{-1}$, consistent with the stretching frequency of the hydrogen-bonded hydroxyl groups, and a sharp band in the $950\text{--}1,200 \text{ cm}^{-1}$ region, arising from the deformation vibration of Sn–OH groups, indicated the presence of CaSn(OH)_6 particles. After calcination, the peaks related to the Sn–OH group and hydrogen-bonded hydroxyl groups disappeared due to the complete dehydration of the precursor [19]. Thus, it was clear that pure

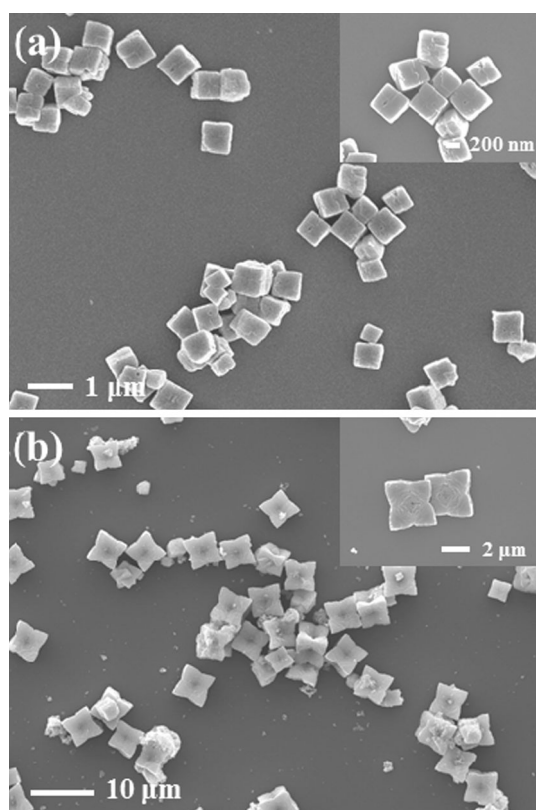


Fig. 4 FE-SEM images of **a** cubic and **b** star-shaped CaSnO_3 particles

CaSn(OH)_6 particles synthesized by the hydrothermal method were converted completely into CaSnO_3 particles by the high-temperature thermal treatment. To assess the chemical composition of the CaSnO_3 particles, XPS measurements were performed and the core-level peaks of Ca $2p$, Sn $3d$, and O $1s$ of the CaSnO_3 particles are shown in Fig. 3. First, the core-level peak of Ca $2p$ exhibited a doublet ($2p_{3/2}$ and $2p_{1/2}$) at 346.1 and 349.6 eV, with a binding energy separation of 3.5 eV. The Sn $3d$ spectrum showed a well-defined doublet ($3d_{5/2}$ and $3d_{3/2}$) at 485.9 and 494.4 eV with a spin–orbit splitting of about 8.5 eV, consistent with a previous report [20]. The O $1s$ spectrum was deconvoluted into two peaks at 529.6 and 531.3 eV, respectively. The main peak at 529.6 eV was attributed to O^{2-} ions of the perovskite anionic network, and the other peak at 531.3 eV was assigned to OH^- and surface-absorbed oxygen. Based on these results, it was confirmed that CaSnO_3 particles were formed, with no apparent chemical modification or change.

Furthermore, the size and morphology of the CaSnO_3 particles was characterized by FE-SEM (Fig. 4). In the case with 5 mL PVP surfactant, cubic-shaped CaSnO_3 particles, with a size of ~ 500 nm, were synthesized (Fig. 4a). However, with 1 mL PVP surfactant added to the synthesis solution, star-shaped CaSnO_3 particles were

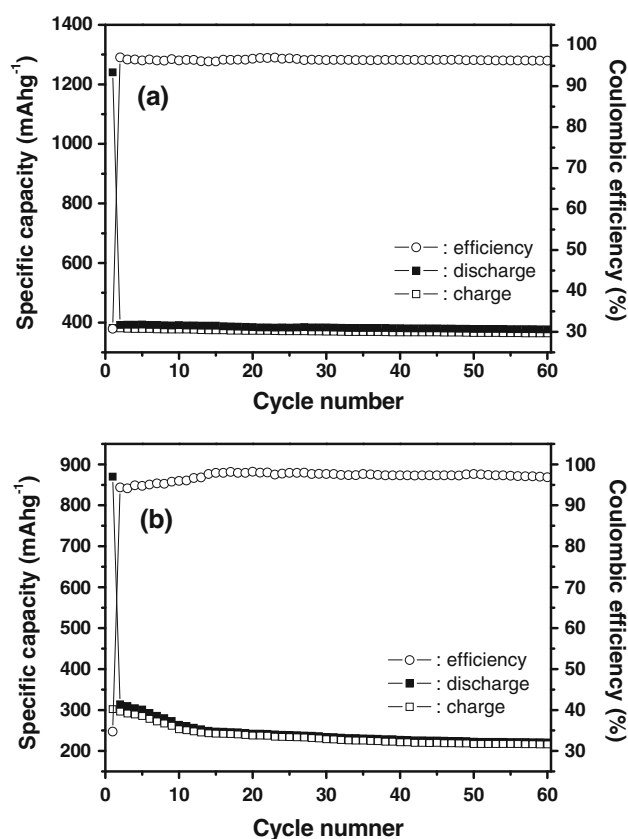


Fig. 5 Cycling performance and coulombic efficiency of **a** cubic and **b** star-shaped CaSnO_3 electrodes at a rate of 50 mAh g^{-1} over the range of 0.0–1.0 V

induced, with a size of $\sim 3 \mu\text{m}$. The magnified view of each image, positioned at the upper right side, confirmed the formation of CaSnO_3 particles with uniform size and sharp corners. The scale of the CaSnO_3 particles was increased greatly with the addition of a small amount of PVP surfactant, and the shape was also modified from cubic to star-shape. Thus, the PVP surfactant played an important role as a shape director where it is selectively adsorbed on the different crystal facets of the CaSnO_3 precursor, preferentially leading to the formation of cubic-shaped particles. It has been reported that with a higher concentration of surfactant, the growth rate of CaSnO_3 particles is reduced [21]. That is, when the amount of PVP surfactant was increased to 5 mL, the crystal growth rate of CaSnO_3 was slower due to the more selective adsorption on the crystal facets of the CaSnO_3 precursor, suppressing the growth rate versus that with 1 mL of PVP surfactant. The resulting cubic CaSnO_3 particles were smaller than the star-shaped CaSnO_3 particles.

Examining the cubic and star-shaped CaSnO_3 particles, their various electrochemical properties were evaluated. Figure 5 shows the cycle capacity and coulombic efficiency of the cubic and star-shaped CaSnO_3 electrodes

during 60 cycles between 0.0 and 1.0 V versus Li^+/Li at 50 mAh g^{-1} . The reversible capacity of the cubic CaSnO_3 electrode was $\sim 370 \text{ mAh g}^{-1}$, showing good cyclability compared with that (302 mAh g^{-1}) of the star-shaped CaSnO_3 . The cubic CaSnO_3 electrode retained its capacity well over the 60 cycles, with 5 % loss relative to the first

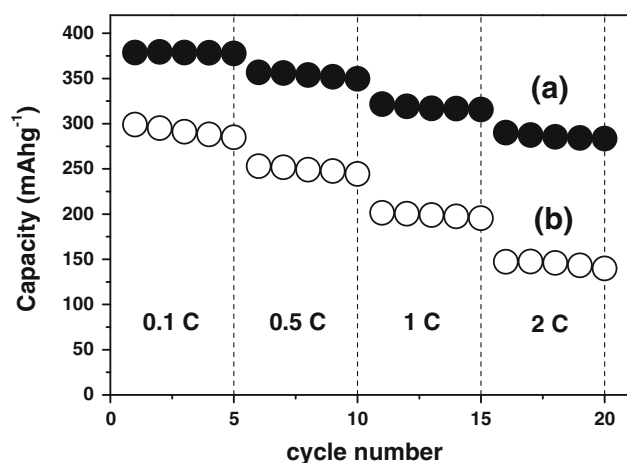


Fig. 6 Rate capabilities of **a** cubic and **b** star-shaped CaSnO_3 electrodes in the potential range from 0.1 to 2.5 V in the different current densities ($1\text{C} = 500 \text{ mAh g}^{-1}$)

cycle capacity, while the reversible capacity of the star-shaped CaSnO_3 decreased continuously in each cycle and showed a 34 % loss relative to the first cycle capacity. Also, the coulombic efficiency of the cubic CaSnO_3 electrode increased from 31 % in the initial cycle to 97 % in the subsequent cycles. The reversible capacity and coulombic efficiency of the cubic CaSnO_3 electrode were stable over 60 cycles, while the star-shaped CaSnO_3 electrode had an irreversible capacity of 870 mAh g^{-1} in the first cycle and subsequently a reversible capacity of 302 mAh g^{-1} , corresponding to a coulombic efficiency of 34 %. During ten cycles, the coulombic efficiency of the star-shaped CaSnO_3 electrode was 94 % in the initial stage, immediately reaching more than 97 % after ten cycles. As the whole, the cubic CaSnO_3 electrode displayed better cycling performance, with a reversible capacity of 370 mAh g^{-1} and coulombic efficiency of 97 %, better than those of the star-shaped CaSnO_3 electrode.

Figure 6 presents the rate performance of cubic and star-shaped CaSnO_3 electrodes in the potential range from 0.0 to 2.5 V and the current densities from 0.1 to 2 C. According to increasing the current densities from 0.1 to 2 C, cubic CaSnO_3 exhibit good rate capacity, achieving the capacity retention of 75 % at 2 C. It may be explained that the excellent rate capability thanks to the sufficient cushioning ability and small size of cubic CaSnO_3 and

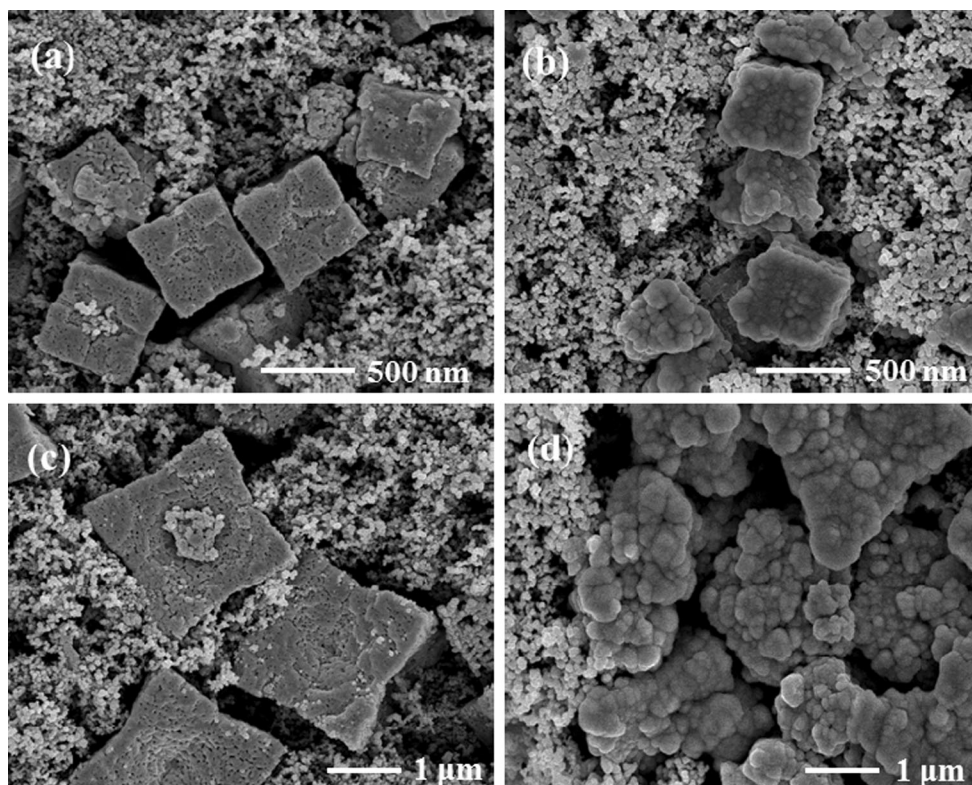


Fig. 7 FE-SEM images of cubic (**a**, **c**) and star-shaped (**b**, **d**) CaSnO_3 electrodes before and after 60 cycles

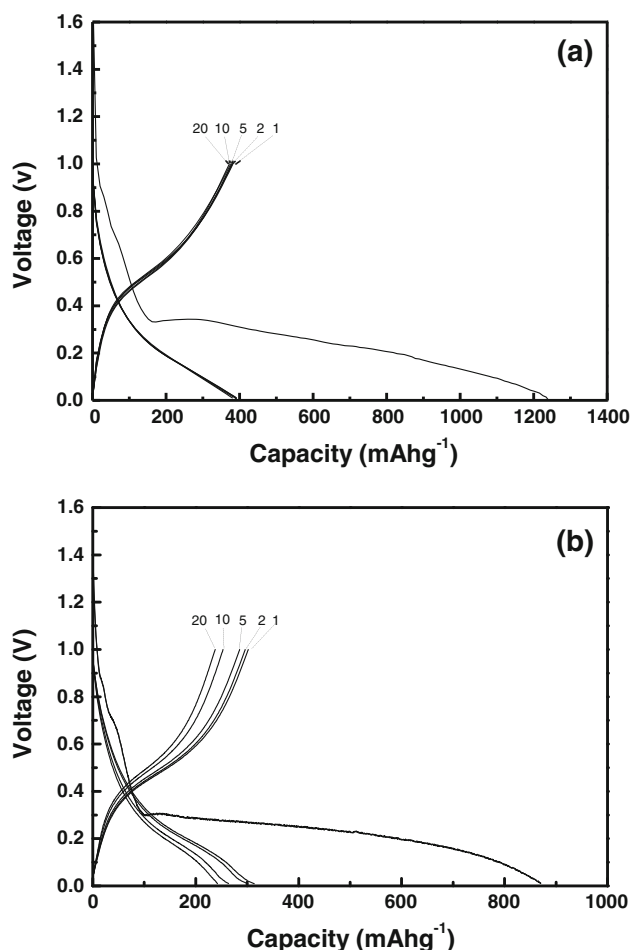


Fig. 8 Charge/discharge curves of **a** cubic and **b** star-shaped CaSnO_3 electrodes

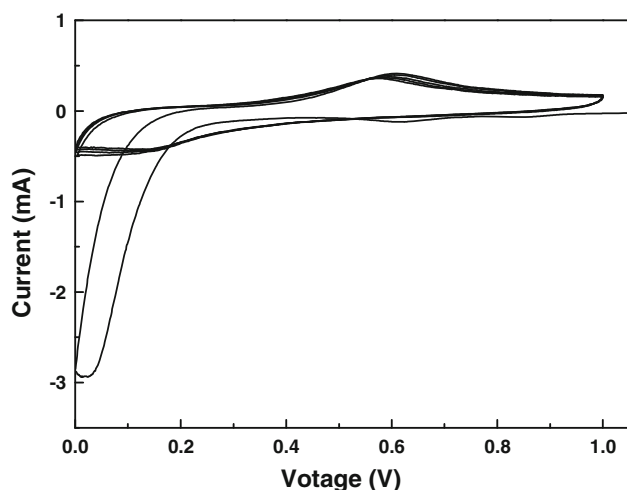


Fig. 9 Cyclic voltammograms of cubic CaSnO_3 electrode with a scan rate of 0.1 mV s^{-1} between 0.0 and 1.0 V

effectively releasing the stress at the interface between Sn active material and CaO phase. However, the star-shaped CaSnO_3 electrode displays the capacity retention of 47 %

at 2 C, probably ascribed to the low cushioning ability of star-shaped CaSnO_3 , resulting in the low rate capability.

Figure 7 compares the morphology of cubic and star-shaped CaSnO_3 electrodes before (a, c) and after 60 cycles (b, d). The cubic CaSnO_3 electrodes retained its original morphology even after 60 cycles (Fig. 7b), while the star-shaped CaSnO_3 electrodes had insufficient cushioning ability to buffer the volume expansion, finally being pulverized. Specifically, the cubic and star-shaped CaSnO_3 particles display a porous structure with the pore diameter of about 20–30 nm. These pores disappeared due to volume expansion after cycling and the cubic CaSnO_3 particles could then soak up the stress from the volume expansion, keeping their original cubic shape during cycling. However, the star-shaped CaSnO_3 particles could not retain their morphology because of the considerable volume expansion. Depending on the material size or the pore size of the star-shaped CaSnO_3 particles, the extent of volume expansion was determined to be a critical factor in determining cycling performance.

The life-cycle performances of the cubic and star-shaped CaSnO_3 electrodes are compared in Fig. 8. The first irreversible capacity loss (788 mAh g^{-1}) was likely caused by the destruction of the lattice, the formation of Sn metal, and the decomposition of the electrolyte, resulting in the formation of a solid electrolyte interphase (SEI) on the electrode surface. The large irreversible capacity of the CaSnO_3 electrode in the first cycle was similar to that of tin oxide (SnO_2), due to the decomposition of SnO_2 into metallic Sn and Li_2O . Generally, the first discharge profile of the SnO_2 electrode shows a typical plateau observed at $\sim 0.9 \text{ V}$, while the CaSnO_3 electrode showed a rather larger plateau at a considerably lower voltage, of $\sim 0.3 \text{ V}$, closely associated with the crystal lattice and the Ca ions in CaSnO_3 [22]. This event was then further examined in the CV analysis. The subsequent charge/discharge cycles show the Sn-alloy reaction in the range of 0.4–0.6 V versus Li/Li^+ , which is similar to the reversible reaction of SnO_2 . Because the reversible voltage profiles reveal stable cycling performance, the reversible capacity for the cubic CaSnO_3 electrode at a constant current density of 50 mAh g^{-1} was 365 mAh g^{-1} , higher than that of 302 mAh g^{-1} for the star-shaped CaSnO_3 after 60 cycles.

Typical CV curves of cubic CaSnO_3 electrodes with a scan rate of 0.1 mV s^{-1} are shown in Fig. 9. The peaks in the CV curves are consistent with the plateaus and sloping potential ranges in the voltage-capacity profiles (Fig. 8). It was readily apparent that the first cycle differed significantly from the subsequent cycles and the main discrepancy was observed in the voltage range of 0.0–0.3 V, attributed to the decomposition of CaSnO_3 and the broad peak that disappeared in the following cycles. Compared with the cathodic peak of $\sim 0.9 \text{ V}$ in the SnO_2 electrode,

the observed cathodic peak at 0.0–0.3 V was significantly low, mainly due to the effect of the crystal lattice and the spectator ion, Ca, in CaSnO_3 [23, 24]. The voltage range of this peak in the first cathodic scan is the same as the plateau region in the initial discharge profile (Fig. 8). The following CV peaks were associated with the reversible Li–Sn alloy formation, which occurs readily during the lithiation and delithiation process. It is evident that the presence of Ca ions induces a change of the CV curve in the first cycle, followed by similar CV curves to those of SnO_2 . Thus, the Ca ions act as spectator ions that do not directly take part in the lithium alloying process due to the high Ca–O bond strength, but provide an additional matrix effect around the Sn metal regions. The role of spectator ions is similar to that of the formation of the Li_2O phase around the Sn metal, such as reactions (1) and (3). The presence of Ca around the Sn metal acts as a physical barrier, hindering the aggregation of Sn particles, as well as a buffering matrix that relieves the volume change during cycling, which also benefits the cycling stability.

4 Conclusions

CaSnO_3 was prepared successfully using a facile hydrothermal method, controlling the amount of PVP surfactant, which has an important role in determining the shape and size of particles. Adding more PVP surfactant to synthesis solution induced the cubic-shaped CaSnO_3 particles, with a size of 500 nm, while less PVP surfactant resulted in the star-shaped CaSnO_3 particles, with a size of 3 μm . The cubic and star-shaped CaSnO_3 electrodes were tested electrochemically for use as anode materials in lithium-ion batteries. From the irreversible capacity of the initial discharge/charge and the reversible capacity, it was shown that the electrochemical properties of the CaSnO_3 electrode were similar to those of Sn-based oxide systems. Also, the shape and size of the CaSnO_3 nanoparticles has a major effect on electrochemical performance. In particular, the cubic CaSnO_3 exhibited better cyclability than that of the star-shaped CaSnO_3 . That is, the star-shaped CaSnO_3 particles were pulverized after 60 cyclings, while the cubic CaSnO_3 particles retained their original morphology and their reversible capacity was above 95 %, even after 60 cycles, demonstrating good cycle performance, attributed to the additional buffering matrix of Ca ions as well as a physical barrier to retard the aggregation of Sn metal. The rediscovery of ternary compound, based on active SnO_2 materials reacting with the lithium ion, may provide an opportunity for the design and development of new anode materials with high capacity and stable cyclability.

Acknowledgments This work was supported by the Institute for Basic Science (IBS) and Fundamental R&D Program for Technology of World Premier Materials and funded by the Ministry of Knowledge Economy, Korea (10037919).

References

- Winter M, Besenhard JO (1999) Electrochemical lithiation of tin and tin-based intermetallics and composites. *Electrochim Acta* 45:31–50
- Wen Z, Lu G, Mao S, Kim H, Cui S, Yu K, Huang X, Hurley PT, Mao O, Chen J (2013) Silicon nanotube anode for lithium-ion batteries. *Electrochem Commun* 29:67–70
- Lee KT, Jung YJ, Oh SM (2003) Synthesis of tin-encapsulated spherical hollow carbon for anode material in lithium secondary batteries. *J Am Chem Soc* 125:5652–5653
- Yan C, Xi W, Si W, Deng J, Schmidt OG (2013) Highly conductive and strain-released hybrid multilayer Ge/Ti nanomembranes with enhanced lithium-ion-storage capability. *Adv Mater* 25:644
- Read J, Foster D, Wolfenstine J, Behl W (2001) SnO_2 -carbon composites for lithium-ion battery anodes. *J Power Sour* 96:277–293
- Yuan L, Konstantinov K, Wang GX, Liu HK, Dou SX (2005) Nano-structured SnO_2 -carbon composites obtained by in situ spray pyrolysis method as anodes in lithium batteries. *J Power Sour* 146:180–184
- Ahn HJ, Choi HC, Park KW, Kim SB, Sung YE (2004) Investigation of the structural and electrochemical properties of size-controlled SnO_2 nanoparticles. *J Phys Chem B* 108:9815–9820
- Courtney I, Dahn JR (1997) Electrochemical and in situ X-ray diffraction studies of the reaction of lithium with tin oxide composites. *J Electrochem Soc* 144:2045–2052
- Brousse T, Retoux R, Herterich U, Schleich DM (1998) Thin-film crystalline SnO_2 -lithium electrodes. *J Electrochem Soc* 145:1–4
- Brousse T, Defives D, Pasquereau L, Lee SM, Herterich U, Schleich DM (1997) Metal oxide anodes for Li-ion batteries. *Ionics* 3:332–337
- Lee JY, Zhang R, Liu Z (2000) Lithium intercalation and deintercalation reactions in synthetic graphite containing a high dispersion of SnO . *Electrochem Solid State Lett* 3:167–170
- Courtney IA, Mekinnon WR, Dahn JR (1999) On the aggregation of tin in SnO composite glasses Caused by the reversible reaction with lithium. *J Electrochem Soc* 146:59–68
- Veeraaghavan B, Durairajan A, Haran B, Popov B, Guidotti R (2002) Study of Sn-coated graphite as anode material for secondary lithium-ion batteries. *J Electrochem Soc* 149:A675–A681
- Li H, Shi L, Lu W, Hung X, Chen L (2001) Studies on capacity loss and capacity fading of nanosized SnSb alloy anode for Li-ion batteries. *J Electrochem Soc* 148:A915–A922
- Sharma N, Shaju KM, Subba Rao GV, Chowdari VBR (2002) Sol-gel derived nano-crystalline CaSnO_3 as high capacity anode material for Li-ion batteries. *Electrochem Commun* 4:947–952
- Lu Z, Liu J, Tang Y, Li Y (2004) Hydrothermal synthesis of CaSnO_3 cubes. *Inorg Chem Commun* 7:731–733
- Fan C, Song X, Yu H, Yin Z, Xu H, Cao G, Zheng D, Sun S (2007) Shape-controlled synthesis of CaSnO_3 micro crystals via a precursor route. *Mater Lett* 61:1582–1588
- Azad A, Liew L, Shyan W, Yen PT (1999) Synthesis, processing and microstructural characterization of CaSnO_3 and SrSnO_3 ceramics. *J Alloy Compd* 282:109–124
- Kutty TRN, Vivekanadan R (1987) BaSnO_3 fine powders from hydrothermal preparations. *Mat Res Bull* 22:1457–1465

20. Sharma N, Shaju KM, Subba Rao GV, Chowdari VBR (2005) Anodic behaviour and X-ray photoelectron spectroscopy of ternary tin oxides. *J Power Sour* 139:250–260
21. Sun YG, Xia YN (2002) Shape-controlled synthesis of gold and silver nanoparticles. *Science* 298:2176–2179
22. Belliard F, Connor PA, Irvine JTS (2000) Novel tin oxide-based anodes for Li-ion batteries. *Solid State Ion* 135:163–167
23. Nam SC, Yoon YS, Cho WI, Cho BW, Chun HS, Yun KS (2001) Enhancement of thin film tin oxide negative electrodes for lithium batteries. *Electrochem Commun* 3:6–10
24. Connor PA, Irvine JTS (2001) Novel tin oxide spinel-based anodes for Li-ion batteries. *J Power Sour* 97–98:223–225